Available online at www.sciencedirect.com
ScienceDirect
Acta Materialia 58 (2010) 2176–2185
Acta MATERIALIA
www.elsevier.com/locate/actamat

Plastic deformation of nanocrystalline aluminum at high temperatures and strain rate

A.P. Gerlich, L. Yue, P.F. Mendez, H. Zhang *

Chemical and Materials Engineering, University of Alberta, Edmonton, Alberta, Canada

Received 31 August 2009; received in revised form 28 November 2009; accepted 2 December 2009
Available online 5 January 2010

Abstract

The deformation of nanocrystalline aluminum was studied using molecular dynamics simulation at homologous temperatures up to 0.97. The microstructures and stress–strain response were examined in a polycrystalline and bicrystal configuration. The activation energies for dislocation-based deformation as well as grain boundary sliding and migration were quantified by fitting simulation data to temperature using an Arrhenius relation. The activation energy for the flow stress response suggests that deformation is largely accommodated by sliding and migration of grain boundaries. This is in agreement with simulated microstructures, indicating a negligible degree of dislocation interaction within each grain, and microstructural observations from high strain rate processes are also consistent with this result. A steady-state grain size is maintained in the recrystallized structure following yielding due to boundary migration and grain rotation mechanisms, rather than by diffusion-based dislocation climb.

Keywords: Nanocrystalline materials; Plastic deformation; High temperature; Molecular dynamics

1. Introduction

Molecular dynamics (MD) simulation has revealed many details of microstructure evolution during plastic deformation. For example, the approach has been used to study the nucleation and annihilation of dislocations at grain boundaries [1,2], the formation of nanotwins [3,4] and the formation of shear bands [5]. The study of nanocrystalline materials by atomic-level simulation has been a particular area of interest, since there has been considerable debate over the deformation mechanisms when the grain size is <100 nm [6]. Recent advances in computing power have enabled simulation of nanocrystalline materials with grain sizes up to 50 nm, and this has been instrumental in clarifying the details of the transition from a dislocation-based to grain boundary-based deformation regime when the grain size decreases [7,8].

Although simulation can provide atomic-level resolution of phenomena during plastic deformation, the short time steps necessitated during calculation have limited investigations to strain rates typically $>10^6\ s^{-1}$. It is still possible to examine lower strain rate deformation such as creep [9], but some special conditions must be imposed in the simulation. On the other hand, the exceptionally high strain rates accessible by MD are directly applicable to a number of processes involving high-temperature deformation. For example, ballistic impacts produce high strain rate deformation ($>10^5\ s^{-1}$), which is often accompanied by the generation of shockwaves and temperatures near the solidus at the projectile interface [10,11]. Strain rates as high as $1600\ s^{-1}$ have been reported in the stir zone during friction stir spot welding [12], and it was shown that the stir zone reaches temperatures of $0.95–0.99T_m$, where T_m is the melting point, in a variety of aluminum alloys [13]. Strain rates of $0.5 \times 10^9\ s^{-1}$ have been suggested at the particle interface during deposition of cold gas dynamic sprayed coatings [14], and it is recognized there is a high

* Corresponding author. Tel.: +1 780 492 8340; fax: +1 780 492 2881.
E-mail address: hao.zhang@ualberta.ca (H. Zhang).

1359-6454/$36.00 © 2009 Acta Materialia Inc. Published by Elsevier Ltd. All rights reserved.
doi:10.1016/j.actamat.2009.12.003

probability of melting at the particle–substrate interface during deposition of aluminum powders [15].

In all of these applications the deformation and recrystallization mechanisms at high temperatures are not fully understood. The Zener–Hollomon relation is widely used to relate strain rate and temperature to a steady-state von Mises flow stress achieved during high-temperature deformation [16] and it has been applied in a variety of numerical modeling applications in order to estimate the mechanical properties at high temperature. One should note that the material parameters have largely been derived from experimental testing in the homologous temperature range of 0.5–$0.9T_m$, at strain rates of 10^{-2}–$10^{2}\ s^{-1}$ [17]. The variations in flow stress and microstructure development in a variety of alloys are explained through dynamic recovery and recrystallization mechanisms driven by dislocation climb, and these account for the decreasing grain or subgrain size with strain rate in the steady-state flow stress regime [17,18]. Depending on the extent of thermally activated coarsening of the grains, extrapolation of the constitutive equations suggests that a nanocrystalline grain size may be achieved with exceptionally high strain rates. This would have great implications for the development of a constitutive equation for flow stress, since dislocation climb-based mechanisms which determine the grain size may not necessarily be extrapolated to the nanocrystalline regime.

In the present work, MD simulations are employed to investigate the deformation mechanisms and microstructure evolution of polycrystalline aluminum under compressive deformation at temperatures close to the melting point. This approach offers the potential to determine the high temperature material properties under conditions that cannot be readily imposed in experiments. To date, the majority of MD simulations have been either conducted at room temperature, did not involve loading to large plastic strains, or focused on a bicrystal geometry. The only MD study of plastic flow at large strains in polycrystalline material has been on creep simulation of Pd up to a temperature of $0.8T_m$ [19]. To the best of our knowledge, the present work is the first to involve MD simulation of deformation of polycrystalline aluminum at a strain rate of $10^{8}\ s^{-1}$ in the temperature range 0.8–$0.97T_m$. The stress–strain response and microstructural evolution are examined in detail, and the activation energies for dislocation and grain boundary-based deformation mechanisms are quantified in order to compare their contributions in this regime.

2. Simulation methodology

A simulation cell of $\langle 0\,0\,1\rangle$ textured microstructure, embedded with four hexagonal grains is considered. As shown in Fig. 1, grain 1 is oriented with crystallographic directions [1 0 0], [0 1 0] and [0 0 1] in the X-, Y- and Z-directions, respectively, while grain 2, grain 3 and grain 4 are rotated around the [0 0 1] tilt axis by misorientation angles of $-27°$, $37°$ and $18.5°$, respectively, resulting in 12 high-

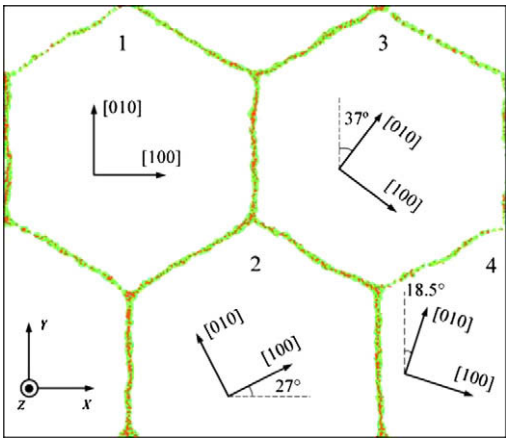

Fig. 1. Initial geometry of grains 1–4, with misorientation angles about the [0 0 1] direction indicated.

angle grain boundaries in the simulation cell. In order to maintain the grain size dependence of yield strength within the normal Hall–Petch relationship [20], an initial hexagonal grain size of 30 nm was selected, while 12 {0 0 1} atomic planes along the Z-direction are chosen to ensure that the thickness is larger than the cut-off radius of the interatomic potential. Based upon these considerations, the simulation cell comprising 582,870 atoms is 69, 60 and 2.4 nm along the X-, Y- and Z-directions, respectively, with periodic boundary conditions.

The atomic interactions are described using the Mendelev et al. [21] form of the embedded atom method (EAM) [22] potential for Al. The simulations are performed within a NPT (fixed number of atoms, pressure and temperature) ensemble, where the constant stress is maintained using the Parrinello–Rahman technique [23] and the temperatures $T = 910$, 891 and 845 K are kept using a rescaling scheme (T_m for this potential is 939 K [21]). Isothermal loading during the compression test prevents any adiabatic effects on the system. It should be also noted that although the rescaling scheme can yield the desired kinetic energy per atom, it does not represent a true constant-temperature ensemble. However, when the system size is large enough and the measured properties are insensitive to temperature fluctuation, the difference between a rescaling scheme and a true canonical ensemble scheme is negligible. In particular, after the initial simulation cell is relaxed under both zero bar pressure and constant-temperature for 200 ps, a uniaxial compressive loading along the X-direction with strain rate of $1 \times 10^{8}\ s^{-1}$ is applied. The Parrinello–Rahman barostat is employed in the Y- and Z-directions to ensure the stress-free state. The atomic stress is calculated using the Virial theorem. MD simulations are performed using LAMMPS [24], developed in the Sandia National Laboratory.

In order to analyze the deformation mechanisms and microstructure evolution, a quantitative measure to distinguish the atoms that belong to grains, grain boundaries and other defects such as stacking faults and vacancies is required. This can be achieved using the bond-order

parameter to identify the local structure around each atom. In this work, the local structure around atom i is determined by the second-order invariant local order parameter [25]:

$$q_l(i) = \left[\frac{4\pi}{2l+1} \sum_{m=-l}^{l} \left| \sum_{j=1}^{N_{nb}(i)} Y_{lm}(r_{ij})/N_{nb}(i) \right|^2 \right]^{1/2}, \quad (1)$$

where Y_{lm} is the spherical harmonics, r_{ij} is the unit vector between atom i and its neighboring atoms j, and $N_{nb}(i)$ is the number of neighbors of atom i. Based upon the values of parameter q_l, different local environments for face-centered cubic (fcc), hexagonal close-packed (hcp) or body-centered cubic (bcc) structures can be determined [25]; consequently, it is possible to distinguish atoms between the perfect crystal, grain boundaries, stacking faults, dislocations and vacancies. Since the deformation simulations are carried out at a temperature close to the melting point (above $0.9T_m$), the thermal fluctuation of each atom makes it difficult to determine the local atomic structure. To remove the thermal fluctuations, the atomic structure was quenched to 0 K, using a conjugate gradient method. It is noted that this energy minimization method only reaches in local potential energy minimum, and therefore does not interrupt the high temperature dynamics. As shown in Fig. 1, those atoms whose local atomic structures are not fcc form a network of grain boundaries (or microstructure).

To study grain boundary self-diffusion, migration and sliding, an individual grain boundary with bicrystal geometry is required. In the present work, a flat Σ5 [0 0 1] asymmetric tilt boundary was chosen as a representation of a high-angle grain boundary (indeed, two of the grain boundaries in the initial polycrystalline microstructure are Σ5 asymmetric tilt boundaries). As shown in Fig. 2, a Σ5 asymmetric tilt grain boundary is constructed by fixing the crystallographic orientations [1 0 0], [0 1 0] and [0 0 1] of the lower grain to the X-, Y- and Z-directions, respectively, and rotating the upper grain around the [0 1 0] axis by 36.9°. Periodic boundary conditions are applied in the X- and Y-directions and the free boundary condition is applied in the Z-direction. In order to simulate grain boundary sliding, a thin layer of atoms near the bottom free surface is fixed by pinning their atomic positions, while the equivalent layer of atoms near the top free surface is displaced along the X-direction at a constant velocity of 1 m s^{-1}.

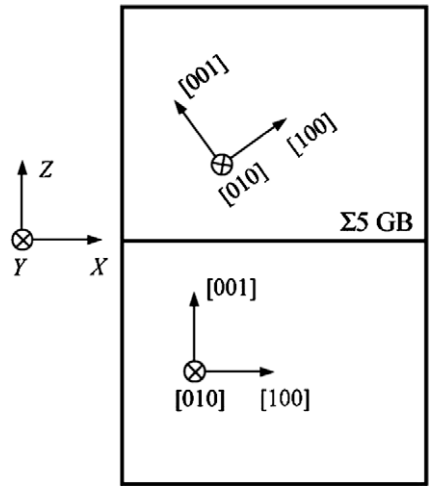

Fig. 2. A schematic bicrystal system used to investigate grain boundary sliding and self-diffusion, where the upper grain is rotated about the [0 1 0] axis by 36.9° to form a Σ5 boundary.

Self-diffusion coefficients are determined using the approach described by Schönfelder et al. [26]. In this method, the grain boundary self-diffusion coefficient is estimated from the slope of the in-plane mean-square-displacement ($\langle(\Delta x)^2\rangle + \langle(\Delta y)^2\rangle$) vs. time. While the boundary may roughen at high temperature, the mean boundary plane is always parallel to the X–Y plane. This approach is, therefore, unaffected by boundary roughening or fluctuation in the mean boundary position. The grain boundary self-diffusivity is as follows:

$$\delta D_{GB} = \frac{\sum_{i=1}^{N_{GB}} (\Delta x_i)^2 + (\Delta y_i)^2}{A} \frac{\Omega}{4t}, \quad (2)$$

where δ, N_{GB}, A and Ω are the grain boundary width, the number of atoms in the grain boundary region, the boundary area and the atomic volume, respectively. Clearly, the definitions of δ and N_{GB} are interrelated as

$$N_{GB} = A\delta/\Omega, \quad (3)$$

and are both arbitrary. If the sum includes a sufficient number of atoms on either side of the boundary, the value of δD_{GB} is independent of δ and N_{GB}.

3. Results

3.1. Microstructural evolution and stress–strain curves

The stress–strain curves obtained during compressive loading at temperatures from 845 to 910 K are shown in Fig. 3. The reduction in the Young's modulus can be readily observed from the decreasing slopes in the elastic region. During the initial elastic loading a peak stress developed, followed by a sharp drop in the compressive stress at around 6% strain. This drop coincided with the break up of the original grains, which initiated in grain 1 shown in Fig. 4. Prior to this, emission of vacancies and dislocations occurs as the yield point is exceeded.

With further strain, all the other grains subdivided until a microstructure with several new grains developed and a relatively steady-state flow stress was reached at strains exceeding approximately 15%. The average flow stresses in the final stages of plastic strain ranged from approximately 250 to almost 800 MPa. Assuming that these average flow stresses obey an Arrhenius relation with temperature, the activation energy for the quasi-steady-state flow stress is approximately 0.95 ± 0.25 eV as shown in the inset of Fig. 3. The ranges in activation energies

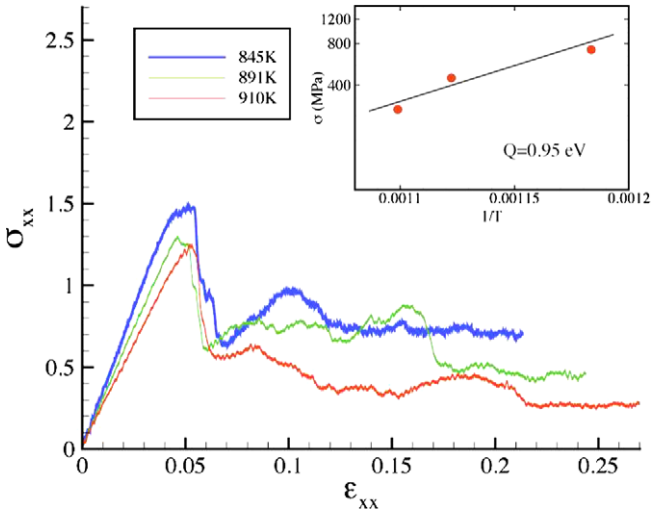

Fig. 3. Stress–strain curves obtained during compressive deformation at temperatures from 845 to 910 K. The relation between the average flow stress during the final 5% strain and $1/T$ is shown in the inset.

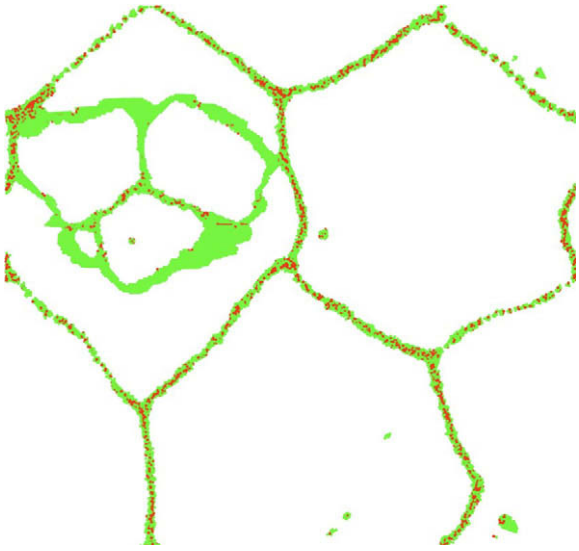

Fig. 4. A snapshot of the microstructure at $0.9T_m$ and approximately 6% strain.

reported in the present work represent the scatter in the regression analysis.

The microstructural evolution during compressive loading from a strain of 16–21% at a temperature of 845 K is shown in Fig. 5. The number of individual grains decreased from 10 to 7, with the average grain size increasing from 20 to 24 nm in the final range of plastic deformation. The grains are elongated in the Y-axis direction as expected for a compressive load parallel to the X-axis. The average size slightly increased in this strain range due to grain growth as well as grain coalescence driven by grain rotation. An example of coalescence can be seen in grains 5 and 6 indicated in Fig. 5, and the misorientation between these grains is shown with increasing strain in Fig. 6. The average misorientation decreases until a low-angle grain boundary with a misorientation angle of $<10°$ is formed between grains 5 and 6, and the original grain boundary is replaced by an array of edge dislocations.

It should be noted that the contributions of coalescence and grain growth at high temperatures are counteracted by grain refinement due to grain subdivision. For example, a grain can be observed subdividing into two grains as a result of a grain boundary migration in the simulation at a temperature of 845 K. The subdivision concludes shortly after a strain of 21%, where the grain boundary ultimately meets a boundary on the opposite side of the grain as indicated by the arrow in Fig. 5.

Compressive loading at a temperature of 910 K results in the formation of grains with an average grain size of 26–29 nm (see Fig. 7). The bond-order parameter used to distinguish the local structure reveals that width of grain boundaries increases with temperature, and that triple junctions and quadruple nodes are formed with dimensions ranging from 5 to 8 nm. These features lead to a drastic increase in the intercrystalline volume fraction near the melting point (see Fig. 8).

3.2. Dislocation emission

Few dislocations were observed within the grains in Figs. 5 and 7. The majority of the disordered clusters of atoms observed within the grains comprised vacancies emitted from grain boundaries due to thermal fluctuations imparted by the high temperatures [27]. A full dislocation is shown following emission from a grain boundary in Fig. 9, while all the other atoms correspond with stacking faults, grain boundaries or vacancies. The presence of a single dislocation within the simulation volume represents a modest dislocation density of about $2.4 \times 10^{14}\ \mathrm{m}^{-2}$. This density produces fewer than one dislocation per grain, which precludes dislocation interactions such as entanglement or the formation of Lomer–Cottrell barriers.

The formation of a stacking fault is shown in Fig. 10. It originates from the grain boundary and nucleates from a grain boundary ledge with a partial dislocation. To quantify the activation energy for dislocation emission and glide during deformation, it is necessary to consider the influence of temperature on both the nucleation and propagation of dislocations. By relating the yield stress shown in Fig. 3 to temperature in an Arrhenius function, the effective activation energy for dislocation emission and glide at these strain rates was determined to be approximately 0.17 ± 0.01 eV.

3.3. Grain boundary sliding

A bicrystal geometry with a flat $\Sigma 5$ [0 0 1] asymmetric tilt boundary was used to study grain boundary sliding at high temperature. A constant strain rate was applied for the geometry shown in Fig. 2, and the stress vs. displacement relationships obtained for temperatures from 750 to 891 K are shown in Fig. 11. At temperatures from 750 to 800 K, the stress increases linearly prior to initiation of

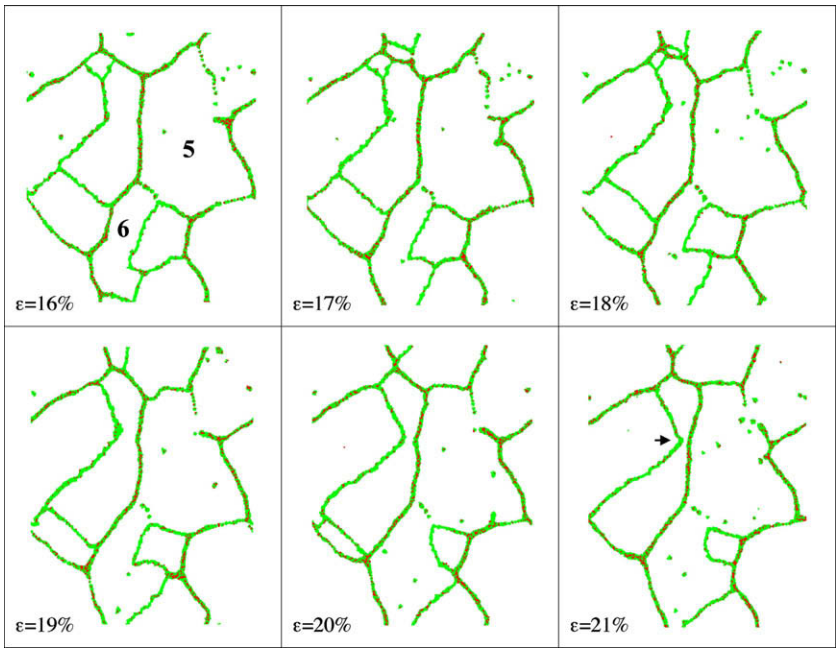

Fig. 5. Microstructural evolution during loading at 845 K, with strains of 16–21%.

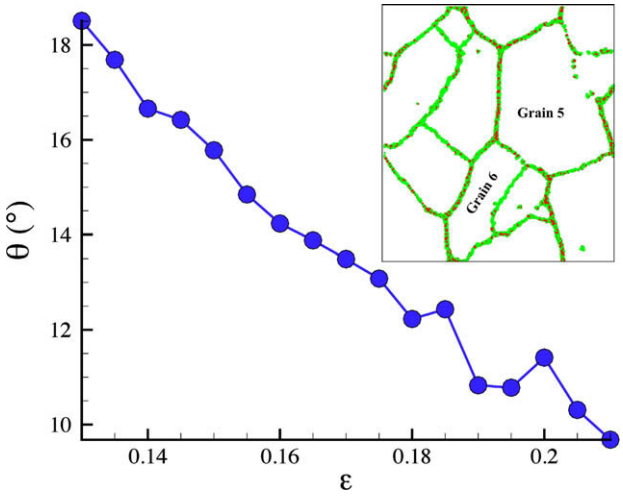

Fig. 6. Grain boundary misorientation between grains 5 and 6 vs. strain during loading at 845 K.

grain boundary sliding, which is followed by a sudden collapse in the stress coinciding with the displacement of atoms across the boundary. At 845 K, the drop in flow stress associated with grain boundary sliding is not as drastic as that at lower temperatures, and instead a gradual decrease occurs followed by a linear increase, leading to another sliding event. When the temperature is 891 K, the stress fluctuations associated with sliding are even smaller; however, peaks can be still be distinguished. Assuming the peak stress required for sliding follows an Arrhenius function with temperature, the apparent activation energy measured for grain boundary sliding is 0.84 ± 0.13 eV, as shown in the inset of Fig. 11.

3.4. Grain boundary diffusion

The bicrystal geometry was examined at high temperatures in order to determine the predominance of mass transport along grain boundaries during high-temperature deformation. The in-plane mean-square-displacement along the grain boundary is shown in Fig. 12 for various temperatures. The approach described by Schönfelder et al. [26] was taken to determine the self-diffusivity of the grain boundary, and the activation energy for self-diffusion is 0.87 ± 0.12 eV, as shown in the inset of Fig. 12.

4. Analysis and discussion

4.1. Steady-state flow stress and grain size

When an Arrhenius relation is fitted to the temperature and steady-state flow stress values shown in Fig. 3, the activation energy parameter is found to be 0.95 eV. This is lower than the measured self-diffusion coefficient for aluminum of 1.48 eV [28], as well as the estimated activation energy for self-diffusion for this potential of 1.62 eV [29]. The activation energies for the temperature dependence of other mechanisms are summarized in Table 1. One would expect the experimentally observed values to be higher, considering the MD simulations are for a perfectly pure metal, and any impurities will drastically increase the activation energy [30]. For example, substitutional impurities are also well known to increase the activation energy for self-diffusion [31].

The activation energy value of 0.17 eV measured for dislocation emission and glide is lower than that observed for

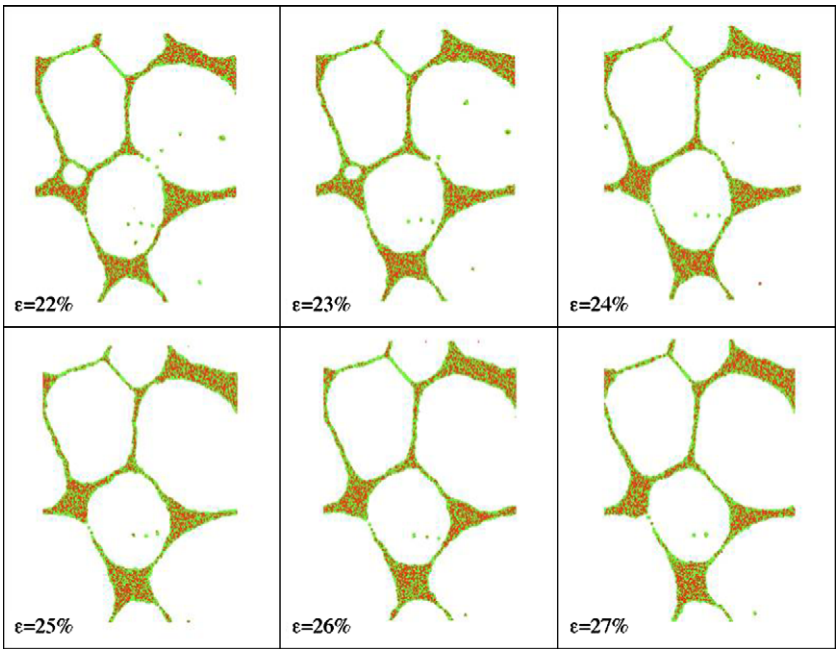

Fig. 7. Microstructural evolution during loading at 910 K with strains of 22–27%.

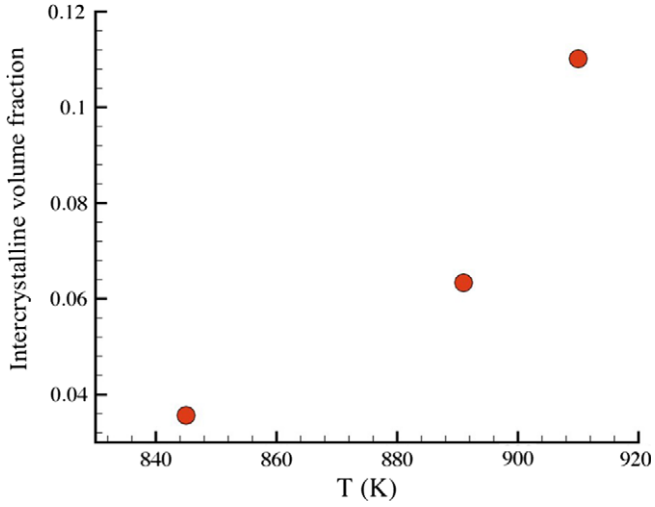

Fig. 8. Intercrystalline volume fraction during quasi-steady-state flow at different temperatures.

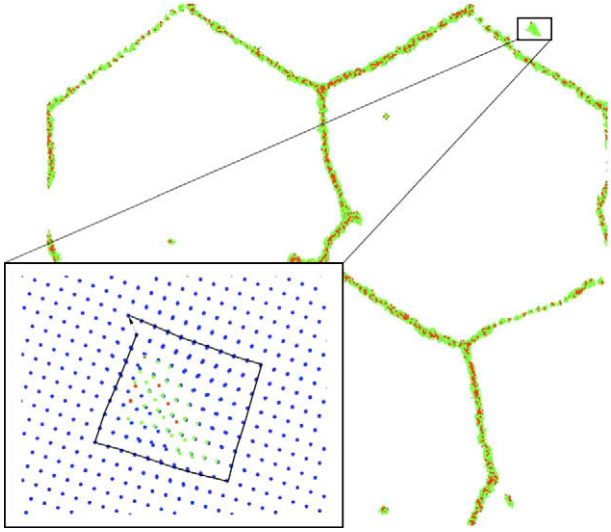

Fig. 9. Details of the atomic arrangement of a dislocation emitted from a grain boundary. The Burgers vector $b = [1\ 1\ 0]a/2$ is shown in the inset.

dislocation migration [32], as well as the value observed for grain boundary migration (0.3 eV) for this potential studied at temperatures up to 850 K [21]. It should be noted that the activation energy for grain boundary migration in copper is also in this range, and that it drops from 0.4 to 0.2 eV at temperatures near the melting point [33]. It was suggested that this change is due to a transition of the migration mechanism from one based on solid-like hopping at low temperatures to liquid-like reshuffling along the grain boundaries. It is suggested that the break up of the initial grain structure is assisted by grain boundary migration, and evidence of migration of the original grain boundaries can be observed in Fig. 4.

A nearly constant grain size is established following yielding as shown in Figs. 5 and 7; however, there is no indication that dislocation climb plays a role in the microstructural evolution at the strain rates and temperatures examined. Grain coarsening could be observed due to the coalescence of grains, as shown in Fig. 6, and the migration of boundaries can also be observed, leading to competitive grain growth of some grains in Figs. 5 and 7. The grain size is maintained in the quasi-steady-state flow region as a result of grain refinement mechanisms which are competing with grain growth and coalescence.

In comparison, the dependence of flow stress on grain size is well known for coarse-grained materials [34] when dynamic recrystallization during high-temperature deformation occurs. This mechanism depends on the generation of a large number of dislocations which climb and

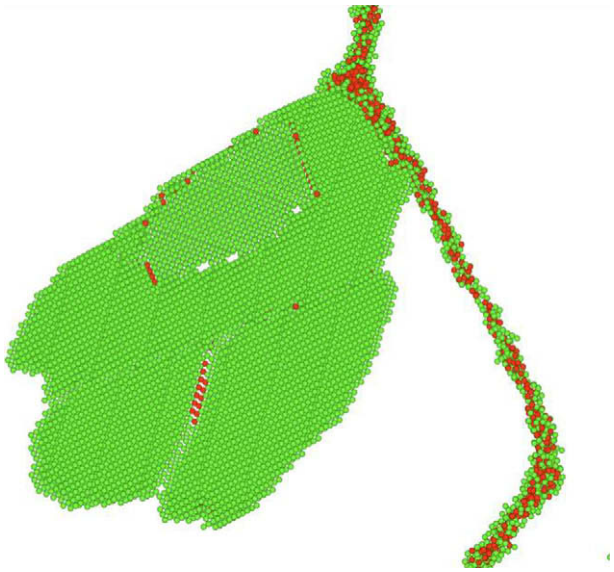

Fig. 10. Stacking fault along a grain boundary at a temperature of 845 K and a strain of 6%.

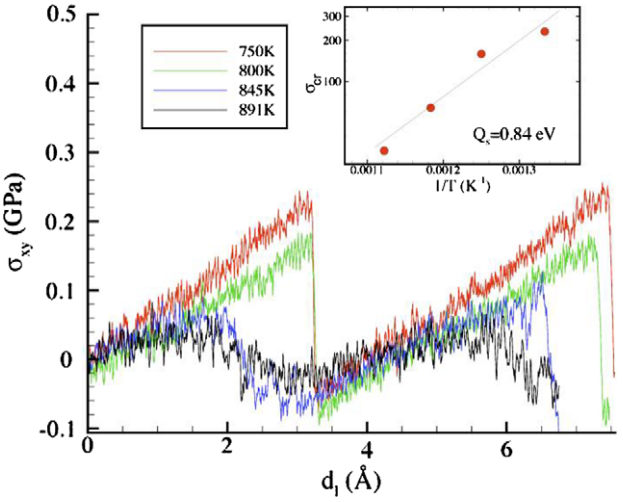

Fig. 11. Stress–strain curves obtained during shearing of a bicrystal at temperatures from 750 to 891 K. The relation between the peak stress required for boundary sliding and $1/T$ is shown in the inset.

ultimately form high-angle grain boundaries which migrate through a deformed microstructure. Once a steady grain size is established, a power law can be used to describe the relationship between flow stress, strain rate and temperature which involves an activation energy parameter for hot working that is typically close to that for self-diffusion in the particular alloy being examined [35]. For example, the hot working activation energy of 99.997% Al was found to be 1.58 eV [36], which is comparable to 0.95 eV calculated from the flow curves produced in the present work.

A unique feature of the recrystallization observed during the MD simulation is that it is not driven by the accumulation of dislocations and dislocation climb (as in the case of traditional hot working), but rather by grain boundary

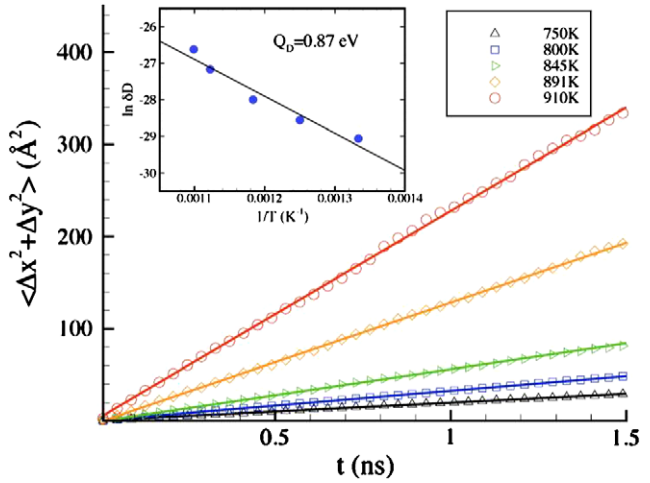

Fig. 12. Mean-square-displacement along the Σ5 [0 0 1] asymmetric tilt boundary vs. time for temperatures from 750 to 910 K.

Table 1
Comparison of activation energies observed for various mechanisms.

Mechanism	Activation energy, eV
Steady-state flow	0.95 ± 0.25
Grain boundary sliding	0.84 ± 0.13
Grain boundary diffusion	0.87 ± 0.12
Grain boundary migration	0.3[a]
Dislocation emission and glide	0.17 ± 0.01

[a] After Ref. [21].

migration. However, the recrystallization process shown in Fig. 5 bears some similarities to geometric dynamic recrystallization which has been proposed during high-temperature deformation of aluminum alloys [37]. Geometric dynamic recrystallization was first described by McQueen et al. [38], and occurs when grains develop serrated boundaries and become elongated due to strain. It is argued that the grain boundary serrations on opposite sides of the grain come into contact with one another, which causes the boundaries to annihilate and will break up the original structure into smaller grains. This recrystallization mechanism has been well studied under torsional loading [39,40]; however, it can also happen under compression [41,42]. Geometric dynamic recrystallization appears to occur in the grain immediately to the left of grain 5 in Fig. 5. During the compressive loading at 845 K, a serrated boundary meets a grain boundary on the opposite side of the grain when the strain reaches 21% (see arrow in Fig. 5), which concludes the geometric dynamic recrystallization process and produces two smaller grains.

4.2. Contribution of dislocations

Less than one full dislocation was observed per grain during simulation as shown in Fig. 9. This supports the notion that deformation is primarily accommodated by intercrystalline mechanisms in nanocrystalline aluminum

at temperatures approaching the melting point. Previous MD simulations involving room temperature deformation of a similar columnar nanocrystalline aluminum grain structure indicated that the deformation process was dominated by grain boundary sliding and diffusion below a critical flow stress of 2 GPa [2]. At the high temperatures investigated here, the flow stress is within the critical range where deformation is dominated by grain boundary mechanisms.

In contrast, this behavior is not generally observed in coarse-grained alloys at room temperature where plasticity occurs by nucleation of dislocations from Frank–Read sources followed by glide of the dislocations along crystallographic slip systems. The size of these dislocation sources cannot exceed the grain size of the polycrystalline material, and the stress required for the Frank–Read source to operate is inversely proportional to the size of the source [43]. As a result, this dislocation nucleation mechanism only operates when grain sizes are larger than about 1 μm, and in nanocrystalline materials dislocations may instead nucleate from grain boundary ledges [44].

The possibility of dislocation emission from grain boundaries has been recognized for some time [45,46], and the details of the process are only recently becoming clear with MD simulation [47–49]. Recently Liu et al. [50] confirmed the formation of partial dislocations and stacking faults near grain boundary and triple junctions in ultrafine-grained Al–Mg alloy following severe plastic deformation. The formation of a partial dislocation at the grain boundary depends upon the absolute value of the stable stacking fault energy and the splitting distance of the leading and trailing partial dislocations [8]. The emission of a partial dislocation from a grain boundary ledge is shown in Fig. 10; however, its propagation is highly dependent on the orientation of the partial dislocation and the geometry of the grain boundary ledge [51].

The value associated with dislocation emission and glide in Table 1 is derived from the yield stress values observed in Fig. 3, and as such it describes the temperature dependence of dislocation emission and propagation at the onset of yielding. The rate of dislocation propagation is correlated to the stress applied, and the Peierls–Nabarro stress is reduced by a factor of $[1 - \alpha\,(u^2/b^2)]$, where α is a numerical factor close to π, u is the mean atomic displacement and b is the Burgers vector [52]. Near the melting temperature the mean atomic displacements increase by some 10–15%, and hence u is at most a few tenths of b according to Lindemann's rule [53]. Consequently, the change in the Peierls–Nabarro stress with temperature will always be negligible, and so it is not surprising that the activation energy calculated for dislocation emission and glide in Table 1 is the lowest of all mechanisms examined. Recent findings also suggest that the emission of a partial dislocation loop at a grain boundary will become a completely mechanically driven a thermal process when the loop radius reaches a critical value [54].

4.3. Grain boundary mechanisms

It has been shown that the dominant deformation mechanisms observed during MD simulations of nanocrystalline materials involve either grain boundary sliding [55–58] or grain boundary diffusion [9]. For example, during grain boundary sliding, stress-assisted free-volume migration and atomic shuffling at the grain boundary are critical in accommodating the deformation [59]. The activation energy calculated for grain boundary sliding (0.84 eV) is lower than the experimental value of 1.50 eV (145 kJ mol^{-1}) for sliding in pure aluminum [60].

Since the grain boundary region is disordered, there is a possibility that grain boundary sliding may be promoted by a transition to a liquid-like state just below the melting temperature [61]. This phenomenon of pre-melting at grain boundary regions has been confirmed in both aluminum and copper [62,63]. Williams and Mishin [64] used MD to examine the thermodynamics of pre-melting and the increase of grain boundary thickness or disorder with temperature. Recently, Zhang et al. [65] has also shown that even at temperatures well below the melting temperature, grain boundaries also behave as glass-forming liquids.

A model for grain boundary sliding in coarse-grained materials at high temperatures and low stresses was proposed by Raj and Ashby [66], and it assumed that deformation is accommodated by liquid films along the grain boundary that promote high diffusion rates. Within the Raj–Ashby model it was assumed that the grain boundary behaves as a thin film of Newtonian liquid with an effective thickness t_{GB}, and viscosity η, so that the shear stress τ required for sliding is:

$$\tau = \upsilon\eta/t_{GB}, \tag{4}$$

where υ is the sliding velocity. The mechanical energy during sliding is dissipated by viscous slip and grain boundary diffusion, where the shear stress required for sliding is inversely proportional to the grain boundary thickness, and the viscosity drops with temperature. Further development of this model has shown that the characteristic time required to equilibrate stresses across the boundary is also inversely proportional to the effective grain boundary thickness [67,68].

The increased grain boundary thickness and diffusion rate, in conjunction with a decreasing effective viscosity of the grain boundary at high temperatures, readily accounts for the drop in flow stress with temperature observed in Fig. 11, in agreement with the Raj–Ashby model. However, the presence of a critical stress suggests that static frictional force must be overcome to initiate sliding. This was also observed by Qi and Krajewski [69] during simulation of grain boundary sliding of an aluminum bicrystal at a temperature of 750 K, and it was suggested the shear stress across the boundary, τ, followed a relation:

$$(\tau - \tau_c) = \upsilon\eta/t_{GB}, \tag{5}$$

where τ_c is the critical shear stress for grain boundary sliding. At temperatures above 800 K, a clear value for τ_c is difficult to discern in Fig. 11. This is likely due to the removal of grain boundary ledges, and the presence of large triple junction regions observed during deformation at 910 K (see Fig. 7). The volume fractions of intercrystalline regions increased drastically up to 11% in this temperature range (see Fig. 8). It should be noted that stress induced pre-melting grain boundaries may also occur, leading to a drastic increase in the grain boundary width [69].

4.4. Comparison to experimentally observed microstructural features

It is difficult to directly compare the simulation results to controlled experiments; however, the microstructures observed during some high-temperature deformation processes provide some support for the proposal that grain boundary-based mechanisms become predominant near the melting temperature. It has been proposed that grain boundary sliding is likely to occur during friction stir welding of Al 2024 alloy, considering that a significant number of dislocation-free grains with dimensions of <250 nm were observed [70]. It was argued that based on the calculated dislocation climb rate it was unlikely for climb and annihilation to account for the low dislocation density in the finest grains, hence the dislocation-free grains could not have been formed by recrystallization. Instead, it is likely that the deformation must be accommodated by grain boundary sliding during the friction stir welding process.

The cold gas dynamic spray process may involve high strain rates near the melting point since metal powders are accelerated at supersonic speeds at a substrate in order to deposit a coating. It is believed that melting at the particle–substrate interface occurs in low melting point alloys due to the high kinetic energies produced [15,71]. Although some transmission electron microscopy studies have been used to characterize cold-sprayed aluminum coatings [72,73], limited examination has been done of the dislocation structures produced in these materials. The microstructures produced in cold gas dynamic sprayed commercially pure aluminum is shown in Fig. 13. Dislocations were seldom found in grains with dimensions <250 nm, while grains with sizes >500 nm did contain high dislocation densities, and a similar trend was observed in friction stir spot welded material [70]. Since large plastic strains are produced during particle impact, the deformation of the fine grains may also have been accommodated by grain boundary-based mechanisms. It is interesting to note that in the case of friction stir welding as well as cold gas dynamic spraying, the critical size for dislocation-free grains appears to be around 250 nm. This suggests the possibility that a transition to grain boundary–dominated mechanisms occurs at much larger sizes when the temperature is near the solidus, compared to the <50 nm transition region reported at room temperature [7,8]. This may be explained by the significant increase in intercrystalline volume fraction at high temperature.

5. Conclusions

Deformation of nanocrystalline aluminum at temperatures of 0.8–0.97T_m appears to be controlled by grain boundary mechanisms. Following yielding, a steady-state flow stress and grain size are developed which depend on the deformation temperature. Although this is well known during dynamic recrystallization of conventional coarse-grained materials as a result of diffusion-controlled dislocation climb, the present work suggests there is negligible dislocation activity in the nanocrystalline grain size range considered. The activation energies for grain boundary-based deformation mechanisms were comparable to the apparent activation energy derived for hot working during simulation. This suggests that the flow stress and grain size is primarily controlled by grain boundary sliding, migration and rotation, rather than diffusion-based dislocation climb. The negligible degree of dislocation activity observed is consistent with deformation microstructures observed in materials produced by high strain rates near the melting tem-

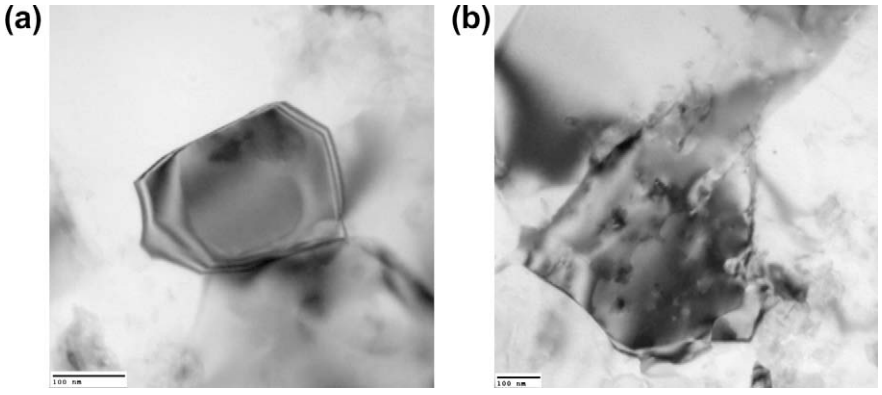

Fig. 13. Transmission electron micrographs of cold gas dynamic sprayed Al powder showing (a) 200 nm diameter grain with no dislocations, and (b) 500 nm grain containing several dislocations.

perature during cold gas dynamic spray coating and friction stir welding.

Acknowledgement

The authors gratefully acknowledge the support of the Natural Sciences and Engineering Research Council of Canada, through the Discovery Grant program.

References

[1] Van Swygenhoven H, Caro A. Appl Phys Lett 1997;71:1652.
[2] Yamakov V, Wolf D, Salazar M, Phillpot SR, Gleiter H. Acta Mater 2001;49:2713.
[3] Yamakov V, Wolf D, Phillpot SR, Mukherjee AK, Gleiter H. Nat Mater 2002;1:45.
[4] Bilde-Sorensen JB, Schiotz J. Science 2003;300:1244.
[5] Hasnaoui A, Van Swygenhoven H, Derlet PM. Phys Rev B 2002;66:184112.
[6] Koch CC, Suryanarayana C. In: Li JCM, editor. Microstructure and properties of materials, vol. 2. Singapore: World Scientific; 2000. p. 380.
[7] Yamakov V, Wolf D, Phillpot SR, Mukherjee AK, Gleiter H. Phil Mag Lett 2003;83:385.
[8] Yamakov V, Wolf D, Phillpot SR, Mukherjee AK, Gleiter H. Nat Mater 2004;3:43.
[9] Keblinski P, Wolf D, Gleiter H. Interface Sci 1998;6:205.
[10] Meyers MA. Dynamic behavior of materials. New York: Wiley; 1994.
[11] Meyers MA, Murr LE, United States. Army research office. Metallurgy and materials science division. Shock waves and high-strain-rate phenomena in metals: concepts and applications. In: Proceedings of an international conference on metallurgical effects of high-strain-rate deformation and fabrication, June 22–26, 1980. Albuquerque (NM): Plenum Press; 1981.
[12] Gerlich A, Su P, Yamamoto M, North TH. J Mater Sci 2007;42:5589.
[13] Gerlich A, Yamamoto M, North TH. J Mater Sci 2008;43:2.
[14] Assadi H, Gartner F, Stoltenhoff T, Kreye H. Acta Mater 2003;51:4379.
[15] Papyrin AN. Cold spray technology. Amsterdam: Elsevier; 2007.
[16] McQueen HJ, Jonas JJ. Recovery and recrystallization during high temperature deformation. Treatise on materials science and technology, vol. 6. New York: Academic Press; 1975. p. 393.
[17] McQueen HJ. Miner Met Mater Soc 2002:345.
[18] Sellars CM, Tegart WJM. Int Met Rev 1972;17:1.
[19] Haslam AJ, Yamakov V, Moldovan D, Wolf D, Phillpot SR, Gleiter H. Acta Mater 2004;52:1971.
[20] Schiotz J, Jacobsen KW. Science 2003;301:1357.
[21] Mendelev MI, Srolovitz DJ, Ackland GJ, Han S. J Mater Res 2005;20:208.
[22] Foiles SM, Baskes MI, Daw MS. Phys Rev B 1986;33:7983.
[23] Parrinello M, Rahman A. J Appl Phys 1981;52:7182.
[24] Plimpton S. J Comput Phys 1995;117:1.
[25] Steinhardt PJ, Nelson DR, Ronchetti M. Phys Rev B 1983;28:784.
[26] Schonfelder B, Wolf D, Phillpot SR, Furtkamp M. Interface Sci 1997;5:245.
[27] Millett PC, Desai T, Yamakov V, Wolf D. Acta Mater 2008;56:3688.
[28] Mohamed FA, Langdon TG. Metall Trans 1974;5:2339.
[29] Mendelev MI, Bokstein B. Mater Lett 2007;61:2911.
[30] Wilshire B, Owen DRJ. Proceedings of the second international conference on creep and fracture of engineering materials and structures. Swansea: Pineridge; 1984.
[31] Shewmon PG. Diffusion in solids. Warrendale (PA): Minerals, Metals & Materials Society; 1989.
[32] Godiksen RBN, Schmidt S, Jensen DJ. Model Simul Mater Sci Eng 2008:16.
[33] Schonfelder B, Keblinski P, Wolf D, Phillpot SR. In: Lejcek P, Paidar V, editors. On the relationship between grain-boundary migration and grain-boundary diffusion by molecular-dynamics simulation, vol. 294–2. Zurich: Trans Tech; 1999. p. 9.
[34] Derby B. Acta Metall Mater 1991;39:955.
[35] McQueen HJ, Ryan ND. Mater Sci Eng A–Struct 2002;322:43.
[36] McQueen HJ, Ryum N. Scand J Metall 1985;14:183.
[37] Solberg JK, Mcqueen HJ, Ryum N, Nes E. Philos Mag A 1989;60:447.
[38] McQueen HJ, Knustad O, Ryum N, Solberg JK. Scripta Metall 1985;19:73.
[39] Kassner ME, Mcmahon ME. Metall Trans A 1987;18:835.
[40] Kassner ME, Myshlyaev MM, Mcqueen HJ. Mater Sci Eng A–Struct 1989;108:45.
[41] Gifkins RC. Strength of metals and alloys (ICSMA 6). In: Proceedings of the 6th international conference, Melbourne, Australia, August 16–20, 1982. Oxford: Pergamon Press; 1983.
[42] Humphreys FJ. In: Gifkins RC, editor. Strength of metals and alloys. Oxford: Pergamon Press; 1982. p. 625.
[43] Cottrell AH. Dislocations and plastic flow in crystals. Oxford: Clarendon Press; 1961.
[44] Li JCM. Acta Metall Mater 1960;8:296.
[45] Mott NF. J Inst Met 1946;72:367.
[46] Hirth J. Metall Trans 1972;3:3047.
[47] Froseth AG, Derlet PM, Van Swygenhoven H. Appl Phys Lett 2004;85:5863.
[48] Van Swygenhoven H, Derlet PM, Froseth AG. Acta Mater 2006;54:1975.
[49] Van Swygenhoven H, Derlet PM, Froseth AG. Nat Mater 2004;3:399.
[50] Liu MP, Roven HJ, Murashkin M, Valiev RZ. Mater Sci Eng A–Struct 2009;503:122.
[51] Van Swygenhoven H. Nat Mater 2006;5:841.
[52] Friedel J. Dislocations. Oxford: Pergamon Press; 1964.
[53] Lindemann FA. Phys Z 1910;11:609.
[54] Asaro RJ, Suresh S. Acta Mater 2005;53:3369.
[55] Zhu YT, Langdon TG. Mater Sci Eng A–Struct 2005;409:234.
[56] Schiotz J, Di Tolla FD, Jacobsen KW. Nature 1998;391:561.
[57] Van Swygenhoven H, Spaczer M, Caro A. Acta Mater 1999;47:3117.
[58] Schiotz J, Vegge T, Di Tolla FD, Jacobsen KW. Phys Rev B 1999;60:11971.
[59] Van Swygenhoven H, Derlet PM. Phys Rev B 2001;64:224105.
[60] Langdon TG. Acta Metall Mater 1994;42:2437.
[61] Ubbelohde AR. The molten state of matter: melting and crystal structure. Chichester: John Wiley; 1978.
[62] Chaudron G, Lacombe P, Yannacquis N. CR Acad Sci (Paris) 1948:1372.
[63] Inoko F, Hama T, Tagami M, Yoshikawa T. Ultramicroscopy 1991;39:118.
[64] Williams PL, Mishin Y. Acta Mater 2009;57:3786.
[65] Zhang H, Srolovitz DJ, Douglas JF, Warren JA. Proc Natl Acad Sci USA 2009;106:7735.
[66] Raj R, Ashby MF. Metall Trans 1971;2:1113.
[67] Mosher DR, Raj R. Acta Metall Mater 1974;22:1469.
[68] Raj R. Metall Trans A 1975;6:1499.
[69] Qi Y, Krajewski PE. Acta Mater 2007;55:1555.
[70] Gerlich AP, Shibayanagi T. Scripta Mater 2009;60:236.
[71] Papyrin AN, Kosarev VF, Klinkov SV, Alkhimov AP. ITSC Proc.; 2002. p. 380.
[72] Balani K, Agarwal A, Seal S, Karthikeyan J. Scripta Mater 2005;53:845.
[73] Ajdelsztajn L, Jodoin B, Kim GE, Schoenung JM. Metall Mater Trans A 2005;36A:657.